# Effective shell wall thickness of vertically aligned ZnO-ZnS core-shell nanorod arrays on visible photocatalytic and photo sensing properties

Kugalur Shanmugam Ranjith[a], Rutely Burgos Castillo[b], Mika Sillanpaa[b], Ramasamy Thangavelu Rajendra Kumar[a,c,*]

[a] Advanced Materials and Devices Laboratory, Department of Physics, Bharathiar University, Coimbatore, India
[b] Laboratory of Green Chemistry, School of Engineering Science, Lappeenranta University of Technology, Sammonkatu 12, FI-50130, Mikkeli, Finland
[c] Department of Nanoscience and Technology, Bharathiar University, Coimbatore, India

ABSTRACT

Development of hierarchical core-shell semiconductor heterostructures ensue significant advancement in catalytic functional structures with improvised optical functionalities. Shell wall controlled vertically aligned ZnO-ZnS core-shell nanorod (NR) heterostructures were grown on transparent conductive substrates along the c-axis by sulfidation of aligned ZnO nanorod arrays for visible photocatalytic properties. The effects of the sulfidation time on the morphology, crystalline properties, optical property, photocurrent response, and photocatalytic activity of the catalyst arrays were studied under UV and visible light irradiation. The shell wall thickness of these heterostructures influenced in great extent the effective photo responsive charge separation and improved carrier mobility. ZnO-ZnS core-shell heterostructure having the shell wall thickness of 20 nm has exhibited more efficient visible photocatalytic behavior due to effective separation of carriers and improved visible absorption. On further increasing the wall thickness the catalytic efficiency was reduced due to the poor carrier (hole) mobility in the polycrystalline shell grains which induced the higher recombination rate. Stability and reusability of ZnO-ZnS core-shell nanostructures reveals that the ZnS acted as a protective layer over the ZnO NR arrays. In appraisal with ZnO NR arrays, the control over the shell wall thickness of ZnO-ZnS core-shell NR array attributed to the excellent visible photocatalytic activity and improvised absorption of light in visible region at ZnO-ZnS interface and effective separation of photogenerated electron-hole pairs at ZnO-ZnS heterojunctions.

## 1. Introduction

In recent years, materials with controlled and systematic assembled structural one dimensional (1D) nanostructures were devised for their novel physical and chemical properties which make them materials of immense potential in different high end applications such as gas and chemical sensing, [1,2] solar cell, [3] photodiodes, [4] field-effect transistors, [5] Schottky diodes, [6] and photocatalyst. [7,8] Concern over the advanced oxidization process (AOP) for the impact on environmental remediation based applications, semiconducting nanomaterials such as ZnO and TiO$_2$ has played a vital role on degrading the organic pollutants. Even though these semiconductors were highly active for the production of reactive oxygen species and effective photocatalytic process under UV irradiation, they were not active under visible irradiation because of their wide band gap. In the form of one dimensional (1D) nanoscale building blocks with tunable dimension and structure complexity will essentially play a multi-functional realization over the tunable photo responsivity with higher surface area but still, it won't impact on the visible absorbance. But, the effective applicability for water splitting through advanced oxidization process on 1D hierarchical arrays promises the production of photo responsive charge carriers and high surface-to-volume ratio with stable reusability in immobilized form of catalytic arrays [9]. In addition, aspects on doping and decorating of the metal ions were influenced over the visible photocatalytic properties by improving the carrier mobility and narrowing the band function. But at the same time these impurities played a role over the host lattice because of the sites recombination's effect decreasing both the carrier separation ratio and the catalytic efficiency. Decorating the narrow band semiconductor layer over the wide band semiconductors in the form of core-shell assembly improvised the carrier separation and delayed the recombination rate by the separation of carriers between the core-shell interface which improved the visible absorption by tagging the narrow band gap semiconductor with the type II form of core-shell assembly [10–12].

* Corresponding author at: Department of Nanoscience and Technology, Bharathiar University, Coimbatore, India.
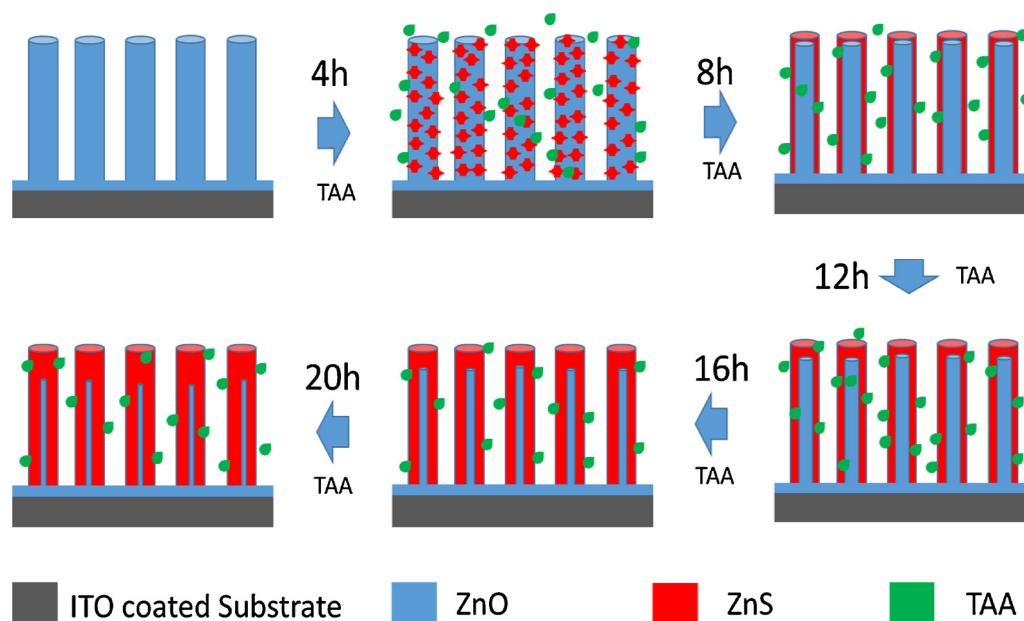*E-mail address:* rtrkumar@buc.edu.in (R.T. Rajendra Kumar).

**Fig. 1.** Schematic representation of the growth of shell wall varied ZnO-ZnS heterostructured photocatalysts.

Therein, construction of vertically aligned 1D hierarchical nanostructures, in form of core-shell nanowires, nanorods, and nanotubes arrays are regarded as promising building blocks for nanoscale devices due to their increased junction area, enhanced polarization dependence and improved carrier confinement with precise electronic properties. Among numerous 1D catalytic platforms that can be used to manipulate the nanostructural system, ZnO NR arrays have been intensively investigated because of their attractive intrinsic properties such as their wide direct band gap (3.4 eV), large exciton binding energy (60 meV), high chemical stability and stable physical properties [13,14]. The wider bandgap of ZnO nanostructures (3.3 eV) can be easily adjusted by creating a narrow band gap shell layer for the effective separation of charged carrier rate with the construction of type II band alignment which poses high lateral charge separation in the core-shell nano structural platform [9,15]. But construction of two wide band gap semiconductors such as ZnO-TiO$_2$, [16] ZnO- SnO$_2$, [17] ZnO-Al$_2$O$_3$, [18] ZnO-ZnS,[19] ZnO-MgO [20,21] in the core shell assembly are also throughly investigated for its tunable optoelectronics and photocatalytic properties.

The shell layer within the core-shell platform acts as a barrier between the core and the environment and can alter the charge, functionality, stability, and reactivity of the core surface. Core-shell structured platform leads to a new form of composite material having properties between the core and shell materials or better than those [22]. But the functional property of the core-shell system will be determined by the shell wall thickness or depletion regions at the core shell interface. So far from the previous investigations, ZnS is often used to modify ZnO surfaces, because of their similar physical properties and to avoid the surface barrier for easier charge transfer. Previous investigations have reported that while decorating the wide band gap semiconductors (ZnO and ZnS) as a core-shell system, at the interface the band function were reduced up to 2.1 eV [23,24]. Recently 1D hierarchical ZnO-ZnS based core-shell structures have garnered much attention for their uses in UV detection, solar cells and even as an efficient visible photo catalyst [19,25,26]. From the early experimental and theoretical predictions, even though the ZnO-ZnS core shell system has the ability to absorb the visible energy at the interface, shell wall thickness will be the crucial factor in order to enhance the efficient charge separation between the ZnS and ZnO. Constructing ZnS based shell layer over the ZnO NR reduces the surface defect states of core system and efficient high quality of hierarchical structure has been

managed [27]. Further this ZnS layer act as a protective layer in order to avoid the corrosion effect on the catalytic surface.

In this study, 1D vertically aligned hierarchical shell wall controlled ZnO-ZnS core-shell nanorods heterostructures were grown on transparent substrates which acted as immobilized hierarchical photocatalysts for catalytic degradation. The motivation of this study is to investigate the visible photocatalytic activity on the hierarchical structure with the influence over the shell wall thickness. Production of reactive oxygen species (ROS), visible photocatalytic response and photo sensing responses were investigated over the ZnO-ZnS core shell system with the influence over different shell wall thickness. Coupling ZnS shell layer with the 20 nm shell wall thickness over vertically aligned ZnO NRs exhibits the enhanced separation of photo induced electron-hole pairs, leading to high photocatalytic efficiency by tunable visible response with faster carrier separation to the surface. Higher shell wall thickness induces higher carrier recombination over the shell wall and the polycrystalline shell grains delay the carrier mobility in the catalytic reaction. By quantifying the production of effective reactive oxygen species (ROS) on the catalytic surface during water splitting under photo irradiation initiates to understand the photo catalytic mechanism influence over the shell wall thickness and the stability over the catalytic arrays promises the ability for the recyclable remediation process.

## 2. Experimental section

### 2.1. Synthesis of vertically aligned ZnO NR arrays

ZnO NR arrays were synthesized by a low temperature aqueous solution growth method. A ZnO buffer layer of ~150 nm thickness was sputtered on glass substrates by DC reactive sputtering (Fig. S1) [28]. For the growth solution, equal moles of zinc nitrate hexahydrate Zn (NO$_3$)$_2$·6H$_2$O and hexamine (HMTA) (C$_6$H$_{12}$N$_4$) were dissolved in double distilled water and stirred continuously for 15 min in separate beakers. The HMTA solution was added dropwise to Zn(NO$_3$)$_2$ solution and stirred continuously for 20 min to form a single phase solution. The buffer layer coated glass substrates were immersed in the growth solution by top facing down and maintained at 97 °C for 4 h. After completing the growth process, the substrates with grown nanostructures were cleaned twice with distilled water and ethanol and dried at 150 °C for 30 mins.
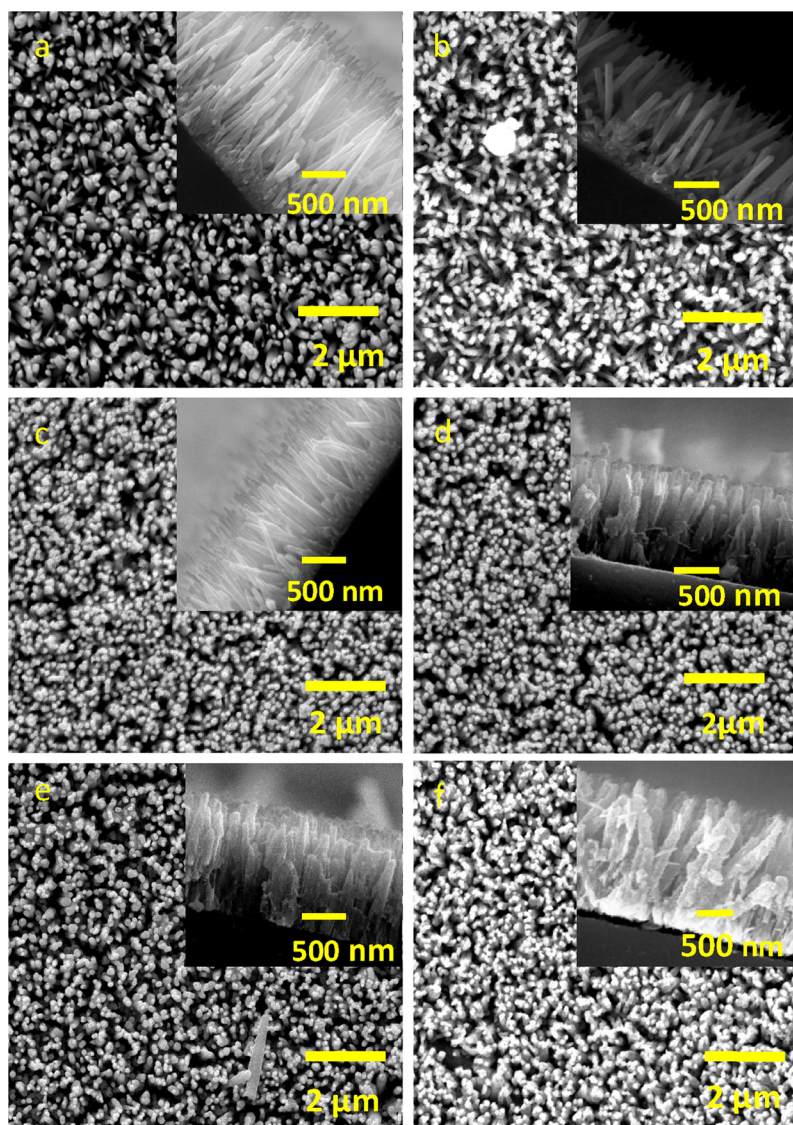
**Fig. 2.** FESEM images showing top view and cross section (inset) of the ZnO-ZnS arrays after different sulfidation time. (a) ZnO-ZnS in 0 h, (b) ZnO-ZnS in 4 h, (c) ZnO-ZnS in 8 h, (d) ZnO-ZnS in 12 h, (e) ZnO-ZnS in 16 h, (f) ZnO-ZnS in 20 h.
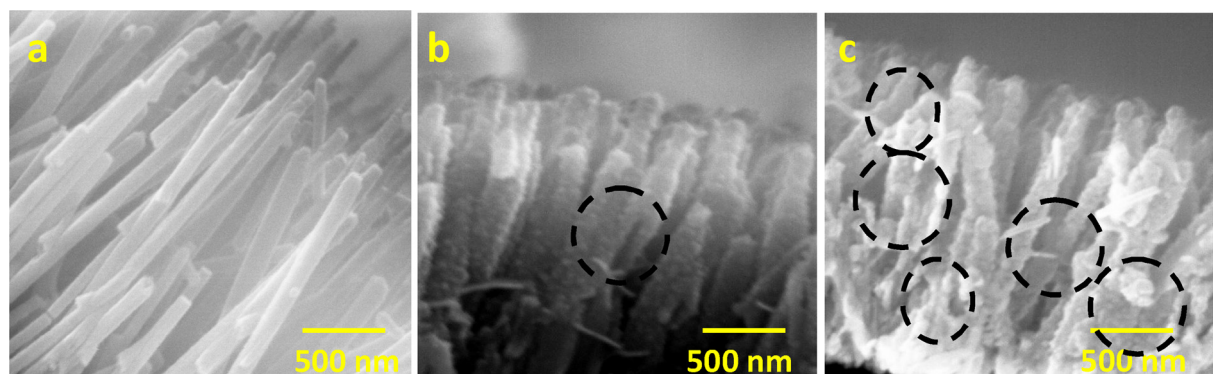


**Fig. 3.** Cross sectional FESEM images of ZnO-ZnS core shell arrays for (a) 0 h, (b) 8 h, (c) 20 h of sulfidation.

### 2.2. Synthesis of vertically aligned ZnO-ZnS core-shell NR arrays

ZnO-ZnS based core shell nanorod arrays were synthesized by controlled sulfidation process. The conversion of the aligned ZnO NR arrays to ZnO-ZnS core-shell NR arrays was carried out by immersing the ZnO NRs array in 30 mM of TAA solution at 60 °C in water bath for different sulfidation times (4 h - 20 h) to create different shell wall thicknesses of ZnS shell layer around the ZnO NRs. After the sulfidation process, substrates were washed with distilled water and then dried at room temperature and annealed for 2 h at 400 °C in nitrogen atmosphere.
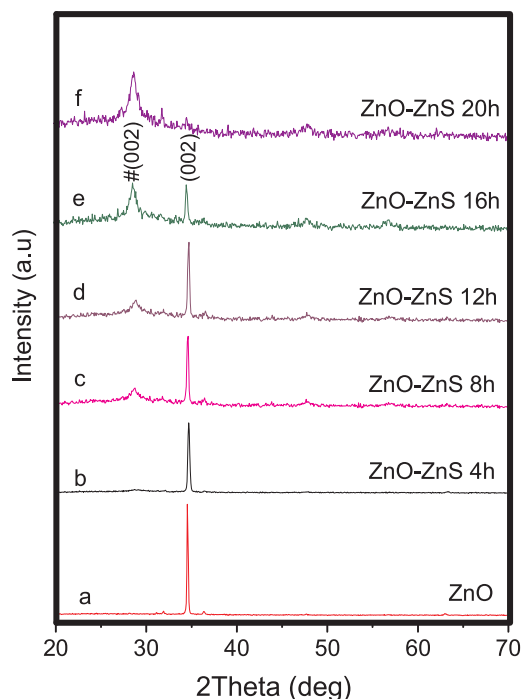
**Fig. 4.** XRD pattern of ZnO-ZnS based core shell NR arrays in different sulfidation time.

## 2.3. Characterization

The surface morphologies and microstructures were analyzed by field-emission scanning electron microscopy (FESEM, QUANTUM) and transmission electron microscopy (TEM, JEOLJEM-2010) equipped with energy-dispersive (EDS) X-ray spectroscopy. The structural properties of the samples were investigated via an X-ray diffraction (XRD, Bruker Advanced D8). The elements present in the hierarchical NR arrays were analyzed by energy-dispersive X-ray spectroscopy (EDS, Oxford Instruments). The diffused reflectance spectra (DRS) of nanocatalytic arrays were obtained using a UV–vis spectrophotometer (UV–vis, Shimadzu). A Perkin Elmer LS 55 fluorescence spectrometer was employed to record the photoluminescence (PL) spectra at room temperature. For the TEM measurement, ZnO-ZnS core-shell nanorods were removed and were dispersed in ethanol via ultrasonication. Then, the samples were collected with carbon copper grids. XPS was performed with a Thermo K-alpha-monochromated spectrometer in constant analyzer energy mode.

## 2.4. Photocurrent test from photo electrochemical (PEC) cells

The PEC measurements were carried out in a quartz cell that can facilitate the transmittance of light onto the surface of photo electrodes when irradiated by a mercury lamp. In order to measure the PEC, the hierarchical NR arrays were grown on the indium tin oxide (ITO) coated glass substrate instead of plain glass substrate. There is no significant change in morphology and alignment of the NR arrays grown on both plain and ITO coated glass substrates (Fig. S2). The surface area of the working electrode is 1.2 cm². The amperometric curves I-t were recorded under an illumination with the simulated sunlight glowed from 75 W Xe arc lamp of intensity 100 mW cm$^{-2}$ for three 30 s light-on-off cycles with 0.1 mol/L Na$_2$SO$_4$ solution as electrolyte, the sample as working electrode and Pt and calomel electrodes acting as the counter and reference electrodes.

## 2.5. Photo degradation of organic dye solution

Photocatalytic activity of the samples was estimated by monitoring the decomposition of Methylene blue (MB) and Rhodamine B (RhB) dyes under 9 W mercury lamp setup with the wavelength of 365 nm (light intensity of 365 lux), 75 W Xe arc lamp setup with simulated sunlight glowed (light intensity of 600 lux) and under natural sunlight irradiation (λ > 400 nm) with a 400 nm cutoff filter having the average visible light intensity of 900 x 100 lux. ZnO based catalyst arrays with the dimension of 1 cm x 1 cm were immersed in 5 ml of 20 ppm MB, RhB dye solutions in quartz cuvettes. Quartz cuvettes with different composition of core-shell NR arrays were placed side by side at the same time and irradiated under sunlight as well as simulated light sources. The catalyst loaded solution was first kept in the dark for 20 minutes to achieve absorption/desorption equilibrium between the catalyst and the dye molecules. As a control experiment, the dye solution without any catalyst was subjected to the same photo treatment in order to compare with the catalyst. The change in absorption peak intensity of MB, RhB at 661 nm and 542 nm respectively, as a function of irradiation time (t) was analyzed via Shimadzu UV-3600 spectrophotometer. The concentration of organic dyes was determined by measuring the absorption intensity at the maximum absorbance wavelength of the supernatant. The degradation percentage (η) of the solutions is defined as follows [29].

$$\eta = \frac{C_0 - C_t}{C_0} \times 100 \tag{(1)}$$

$C_o$ is the initial dye concentration and $C_t$ the dye concentration after an illumination time t (min). The rate of dye degradation ($C/C_0$) is quantified with the first order exponential fit. Additionally, experiments were performed for five consecutive cycles to test the stability and reusability of the photocatalysts. Light intensity was measured every 30 min, and the average light intensity over the duration of each experiment was calculated. The sensor was always set in the position of maximum intensity. The intensity of solar light was measured using a LT Lutron LX-10/A Digital Lux meter and the intensity was 910 × 100 ± 100 lx. The intensity was nearly constant during the experiments.

## 2.6. Active species trapping and superoxide radical quantification experiments

For identifying the active species during the photocatalytic reaction, hydroxyl radicals (°OH), superoxide radicals (O$_2$°) and holes (h$^+$) were investigated by adding 1.0 mM isopropyl alcohol (IPA) (a quencher of °OH), Benzoquinone (BQ) (a quencher of O$_2$°) and triethanolamine (TEOA) (a quencher of h$^+$), respectively [30,31]. The method was similar to the former photocatalytic activity test.

## 3. Results and discussion

The schematic representation of the synthesis of different shell wall thickness of ZnO-ZnS core-shell NR arrays are illustrated in Fig. 1. The exchange of ZnS shell layer over the ZnO NR arrays were follows the surface materializes in three steps. First, TAA reacts with H$_2$O to form CH$_3$(NH$_2$)C(OH)–SH via sulfidation process (Eq. (2)), which further hydrolyzes releasing H$_2$S (Eq. (3)) [32].

CH$_3$CSNH$_2$ + H$_2$O → CH$_3$(NH$_2$)C(OH) + SH …. (2)

CH$_3$(NH$_2$)C(OH)SH + H$_2$O→ CH$_3$(NH$_2$)C(OH)$_2$ + H$_2$S …. (3)
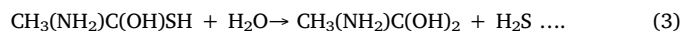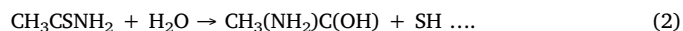
Then, H$_2$S readily reacts with ZnO at the surface of the ZnO NRs to produce ZnS nuclei (Eq. (4)) [32].

H$_2$S + ZnO → ZnS + H$_2$O …. (4)

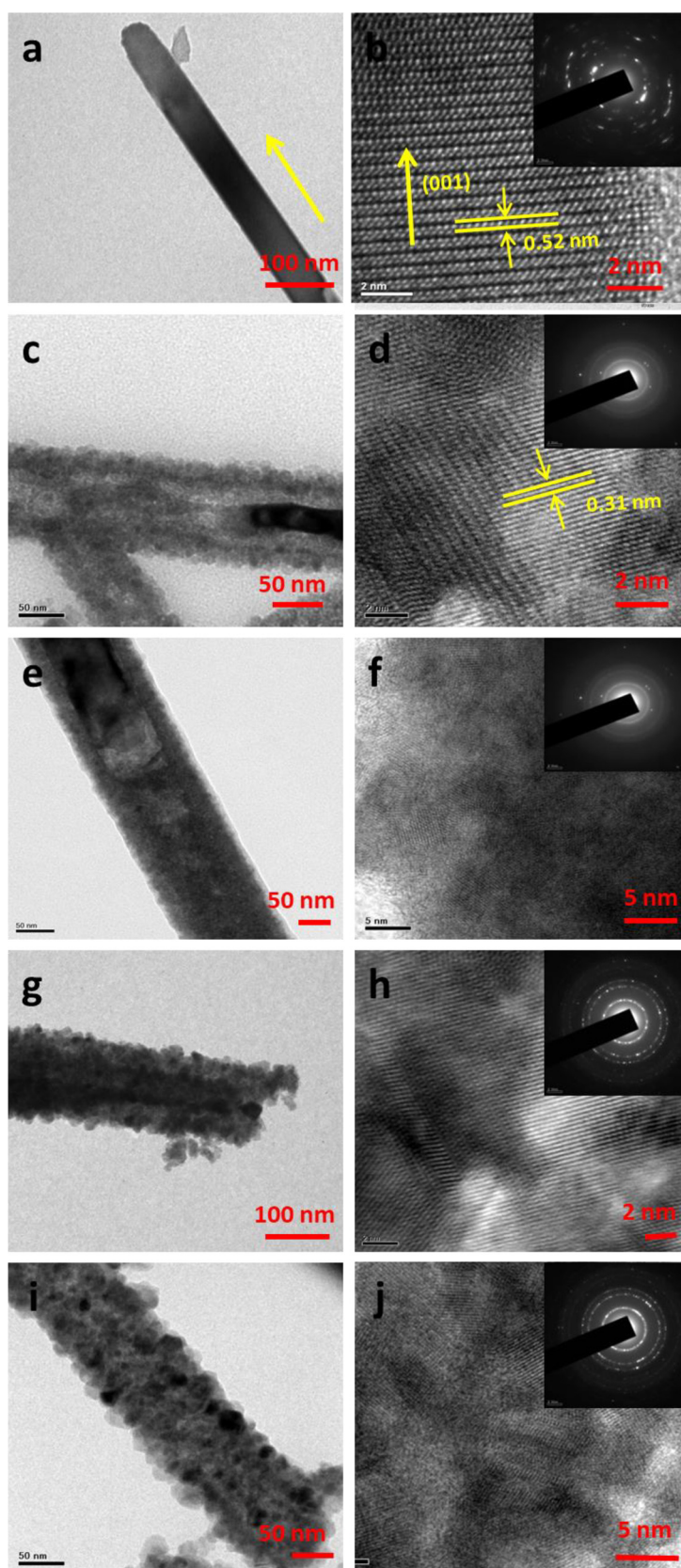Accordingly, heterogeneous nucleation takes place on the surface of

**Fig. 5.** HRTEM images of ZnO-ZnS core shell structures after (a, b) 0 h, (c, d) 4 h, (e, f) 8 h, (g, h) 16 h and (i, j) 20 h of sulphidation. Insert shows the SAD of the respective images.
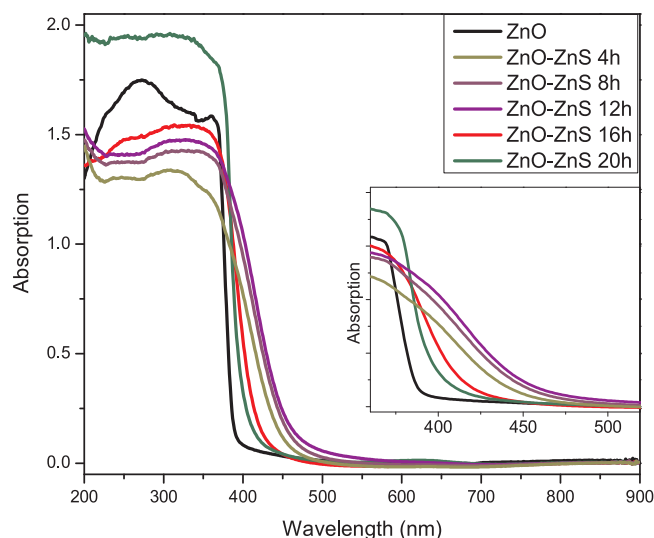
**Fig. 6.** UV DRS absorption properties of shell wall controlled ZnO-ZnS core shell NR arrays.
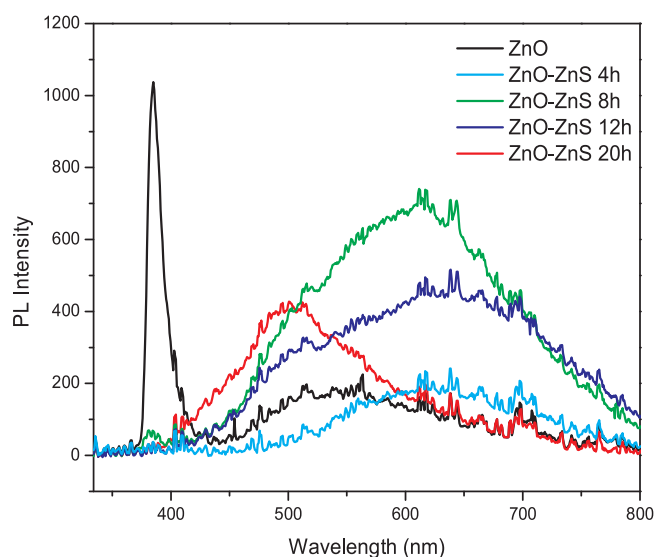


**Fig. 7.** Room temperature photoluminescence spectra of shell wall controlled ZnO-ZnS core shell NR arrays.

the ZnO NRs and a large quantity of ZnS nuclei clinging to the ZnO NRs are produced simultaneously. The heating can improve the nucleation rate for the formation of ZnS nuclei around the sites, which can be catalytic towards the decomposition of TAA [33]. As the reaction proceeds, the ZnS nuclei would grow larger and larger to form ZnS nanoparticles, which finally results in the formation of ZnO-ZnS core-shell NRs. As increasing the reaction time, shell wall thickness over the ZnO-ZnS core shell were increased.

### 3.1. Structural and morphological studies

Fig. 2 show FESEM images of the vertically aligned ZnO and ZnO-ZnS core-shell NR arrays synthesized in different sulfidation time and the inset shows respective cross sectional images of shell wall controlled ZnO-ZnS core-shell NR arrays. Fig. 2a shows a typical FESEM image of as-synthesized vertically aligned ZnO NR array, revealing perpendicular growth of ZnO NRs on the glass substrate with an average length of ∼ 3.5 μm and diameters in the range of 70–90 nm. Fig. 2b-f presents the FESEM images of ZnO NR arrays sulfidated for 4 h, 8 h, 12 h, 16 h and 20 h respectively. Compared to the bare ZnO NR arrays, noticeable

increase in the diameter and rough surface on the sulfidated samples implies that ZnS were decorated over the surface of the ZnO NR. From Fig. 2 (b–e), it can be well-observed that after sulfidation up to 16 h, there is a considerable surface roughness, but no break up in the alignment or destructive change in the morphology of the nanorods. But on prolonging the sulfidation time above 16 h (Fig. 2f), the arrays collapse and the NRs are converted into porous surfaced NRs, as can be clearly seen from the damaged surfaces of NR arrays in Fig. 2f and 3c (dotted circles). In the higher sulfidation time (20 h), some of the shells have an irregular open tip, clearly demonstrating the hollow nature of the prepared NRs and complete transformation of ZnO NRs into ZnS NRs arrays. The formation of ZnS can be explained by the Kirkendall process, which causes due to the diffusive migrations of different atomic species in metals and/or alloys under thermally activated conditions [34] (Fig. 3).

The corresponding X-ray diffraction (XRD) pattern of the bare ZnO NR arrays and ZnO NR arrays grown in different sulfidated hours (4 h-20 h) for ZnO-ZnS core shell formation (clearly evidenced from the FESEM) are shown in Fig. 4(a–f). From curve a, the typical diffraction peaks of strong hexagonal ZnO (002) (JCPDF no. 36-1451) diffraction peak at 2θ = 34.4 is observed in XRD patterns for the bare ZnO NR array, indicating strong preferred orientation along the c-axis of wurtzite (WZ) ZnO. In the case of ZnO-ZnS core shell array, relative intensities of the peaks corresponding to ZnO is found to be reduced due to the formation of outer ZnS shell. Additional peaks corresponding to the lattice planes of hexagonal (0016) phase of ZnS are also observed in the XRD data. When the sulfidation time is 4 h, the diffraction peak of ZnO is still very strong with a very weak peak of hexagonal ZnS (JCPDS 89-2423), as demonstrated in curve b. As the sulfidation time is increased to 8 h, 12 h, the ratio of the characterization peaks of ZnS/ZnO increases (curve c, d), implying that more and more ZnO changes to ZnS with the increasing reaction time. It is also noticed that the relative intensities of ZnS related peak increase on increasing the sulfidation time. This indicates that outer shell layers are getting thicker on increasing the sulfidation time.

On further increasing the sulfidation time up to 20 h, all of the XRD characterization peaks of ZnO disappear and only the diffraction peak of ZnS can be found in the XRD pattern of the final product (curve f), demonstrating that the ZnO NRs are completely converted into ZnS NRs [34]. No additional diffraction peaks other than ZnO and ZnS are observed in the XRD pattern, as the conversion of zinc oxide to zinc sulfide is a diffusion limited process. But from the XRD results, it is clearly observed that the intensity ratio of the peak for the (0016) plane of ZnS to the peak for the (002) plane of ZnO gradually increased with an increase in reaction time. This indicates that the conversion of ZnO crystals to ZnS is continuous with an increased reaction time. But, in our case good control over the ZnS shell thickness on the ZnO core was due to the post annealing after sulfidation process (fig. S3). This is because under the annealing process, the diffusion coefficients of sulfur and oxygen increase, which is necessary for the replacement of oxygen by sulfur. At high temperatures, oxygen atoms obtain sufficient kinetic energy to leave their lattice sites by thermal disturbance, and sulfur atoms are diffused into the ZnO lattices to occupy the oxygen vacancies. [35] The preferred orientation of the ZnO (002) crystal facet through all conversion stages implies that the conversion from ZnO to ZnS takes place on the surface of ZnO columns and continues across the sidewall of the rods.

Fig. 5 shows HRTEM images of shell wall controlled ZnO-ZnS core shell structures after 0 h, 4 h, 8 h, 16 h and 20 h of sulfidation. The sharp interface between the core and shell clearly shows that the ZnO NRs are fully sheathed by a ZnS layer along their entire length. On increasing the sulfidation time, ZnS layer thickness increases and has a poly crystalline grain assembly of rough surface. Fig. 5a and b shows the HRTEM images of as synthesized single crystalline ZnO NR. HRTEM studies show that ZnO NRs are purely single crystalline and grown along 002 direction since the observed d-spacing value of the
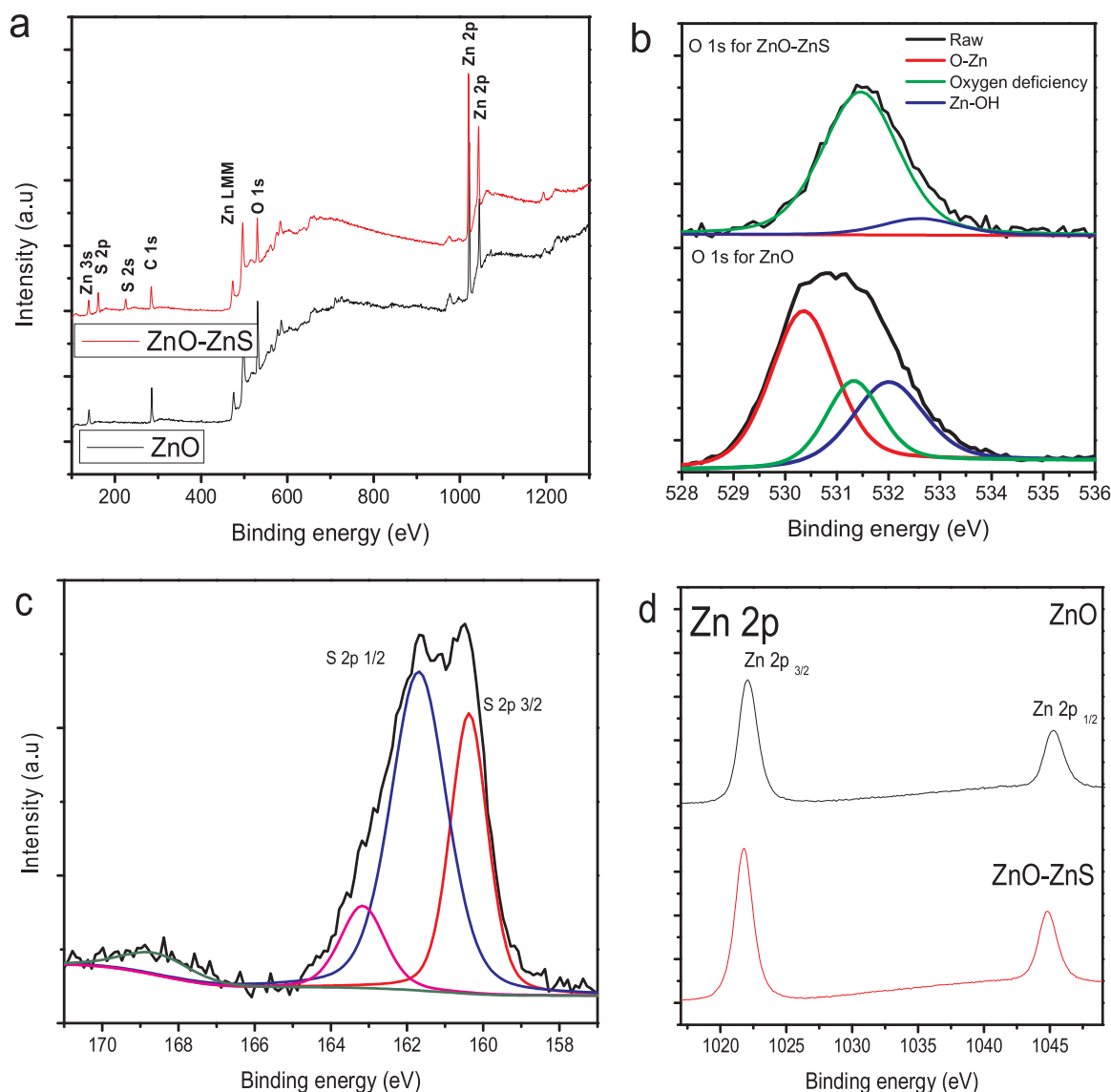
**Fig. 8.** XPS spectra of ZnO and 8 h sulfidated ZnO-ZnS core/shell heterostructure: (a) complete survey and (b) O1s, (c) S2p, and (d) Zn2p peaks.

diffraction fringes is 0.52 nm (Fig. 5b). The contrast difference of the NR confirms the core-shell structure from the Fig. 5c-j which shows the role of sulfidation over ZnO NR in different sulfidation time. On increasing the sulfidation time, shell wall thickness increased as ∼10 nm, ∼20 nm and ∼30 nm for 4 h, 8 h and 16 h of sulfidation respectively. On further increasing the sulfidation time, ZnO core completely diffused to form ZnS indicated by the absence of image contrast of the core shell interface (Fig. 5i). It can be noticed that the shell layer is not continually smooth, rather it is a formation of polycrystalline grains of ZnS, as can be seen from the HRTEM image. To get more information about the growth relationship, magnified HRTEM images of the core and shell taken for the ZnO-ZnS based NRs is given in Fig. 5 (b, d, f, h, j) and their corresponding SAD patterns are shown as inset. The polycrystalline form of ZnS coupled with single crystalline ZnO NR gives evidence to the formation of ZnO-ZnS core shell structures. The marked inter planar d spacing of 0.31 nm corresponds, respectively, to the (111) lattice plane of hexagonal ZnS with the (011) zone axis [36]. To confirm the presence of outer ZnS shell layer further, EDAX elemental analysis are employed across the single core-shell NR, which is shown in Fig. S4 EDAX profile illustrated the presence of higher S concentration on increasing the sulfidation time of the NR.

### 3.2. Optical studies

Fig. 6 shows diffuse reflection spectra of samples that are glass substrates decorated with ZnO and shell wall controlled ZnO-ZnS core-shell nanorods arrays. For the as prepared ZnO sample, the spectrum locates only in the UV range. When ZnS shell layers are grown on the surface of ZnO nanorods, visible light absorption band tail is observed in addition to the band gap absorption band of the ZnO nanorod core. In comparison, increasing the shell layer thickness promotes the UV and visible light absorption properties than that of ZnO NRs.

Fig. 7 shows the room temperature PL spectra of as grown shell wall controlled ZnO-ZnS core-shell structures. To compare the luminescence intensity of the ZnO-ZnS core-shell, PL spectra of bare ZnO is used as a reference. Two emitting bands, including a strong violet emission centered at around 380 nm and a weak green band centered at around 530 nm, are observed in ZnO nanocrystals. The green emission could be attributed due to the defect related emissions between $Zn_i$ and VB; $O_{Vo}$ and VB respectively [37]. The PL spectra of ZnO-ZnS core-shell structures show an enhanced broad violet and orange emission and a disappearing green emission compared to that of ZnO nanocrystals. The effect of shell wall over the ZnO NR arrays shows a distinctly suppressed UV emission with a small red-shift and an enhanced yellow
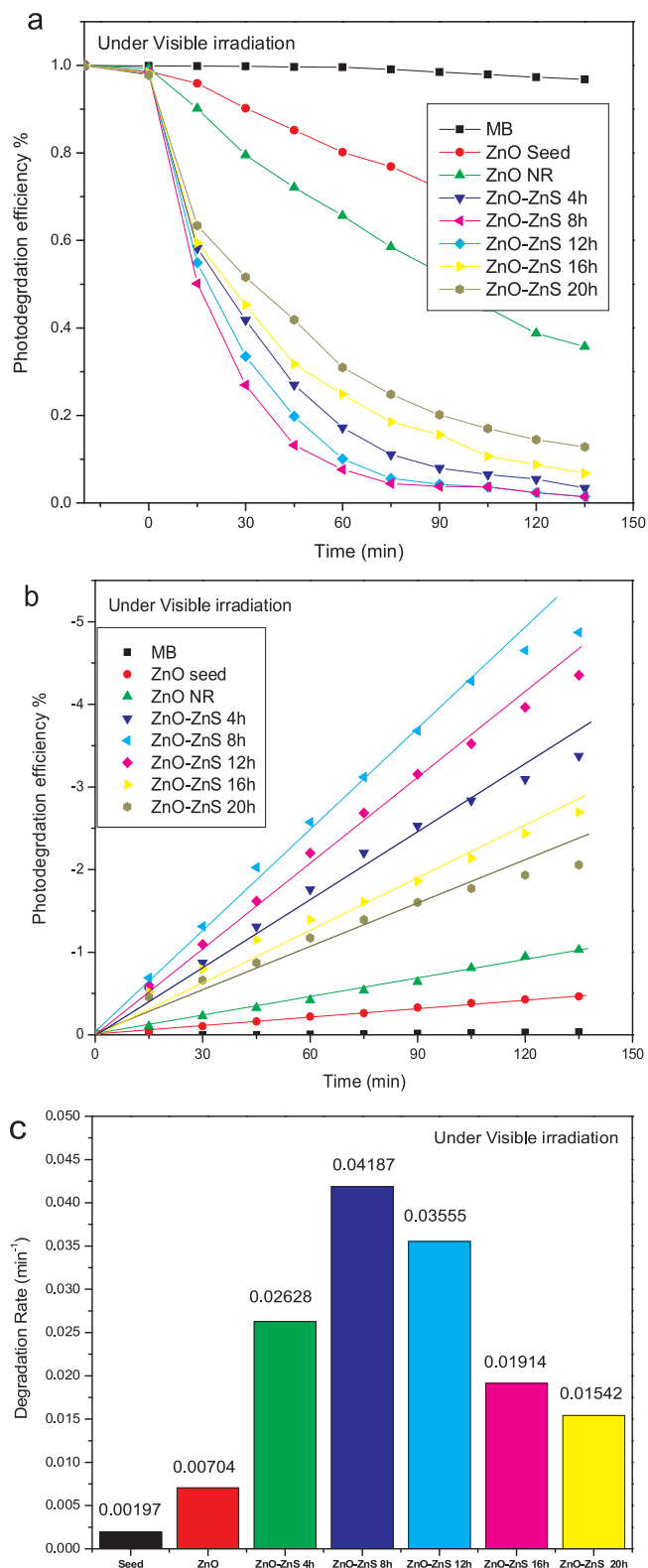
**Fig. 9.** Photocatalytic properties of shell wall controlled ZnO-ZnS based core shell NR arrays under visible irradiation (a) degradation profile (b) first order fit and (c) Comparison study on the photocatalytic degradation rate under.

emission, as compared to that of pure ZnO NRs. The red-shift of the UV emission can be attributed to the strain caused by the lattice mismatch between ZnO and ZnS. As predicted by the previous theoretical works, strain in the ZnO-ZnS interface are strong enough to reduce their total band gap of the system [38]. The broad emission in the visible region

**Table 1**
Photo responsive properties of shell wall controlled ZnO-ZnS based core shell NR arrays.

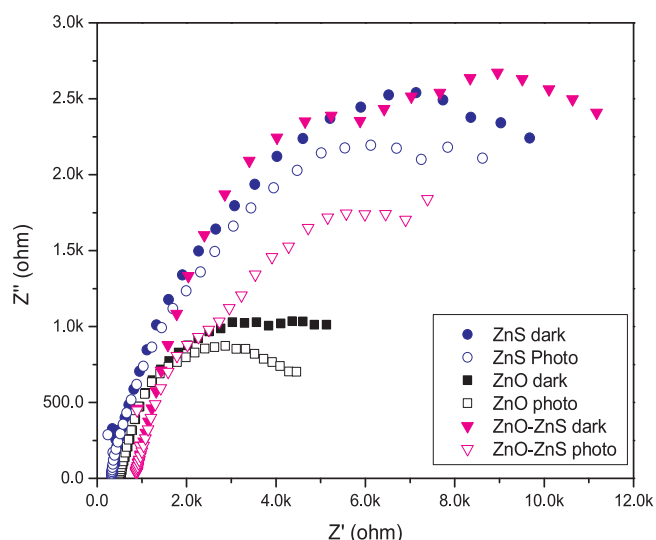| S.No | Hybrid NR arrays | Shell wall thickness | Band edge absorbance | Degradation efficiency under UV in 140 min ($\lambda = 365$ nm) | Degradation efficiency under Visible in 135 min ($\lambda > 400$ nm) | Degradation efficiency under Sunlight in 140 min ($\lambda > 400$ nm) | Degradation Rate (min$^{-1}$) ($\lambda = 365$ nm) | Degradation Rate ($\lambda > 400$ nm) | Degradation Rate under sunlight ($\lambda > 400$ nm) |
|---|---|---|---|---|---|---|---|---|---|
| 1 | Seed | – | 372.12 | 40.44 % | 36.81 % | 13.72 % | 0.00294 | 0.00197 | 0.00121 |
| 2 | ZnO NR | – | 387.72 | 79.11 % | 64.42 % | 56.05 % | 0.01288 | 0.00704 | 0.00637 |
| 3 | ZnO-ZnS 4 h | ~10 nm | 455.55 | 82.23 % | 96.32 % | 78.03 % | 0.01509 | 0.02628 | 0.01021 |
| 4 | ZnO-ZnS 8 h | ~20 nm | 460.51 | 89.62 % | 98.74 % | 94.66 % | 0.02047 | 0.04187 | 0.02248 |
| 5 | ZnO-ZnS 12 h | ~25 nm | 457.71 | 87.64 % | 98.21 % | 91.53 % | 0.01855 | 0.03555 | 0.01878 |
| 6 | ZnO-ZnS 16 h | ~30 nm | 415.83 | 84.27 % | 93.91 % | 84.27 % | 0.01538 | 0.01914 | 0.01461 |
| 7 | ZnO-ZnS 20 h | >40 nm | 398.43 | 69.26 % | 87.43 % | 69.26 % | 0.01018 | 0.01542 | 0.00868 |

**Fig. 10.** Nyquist plots of the EIS of pristine ZnO, ZnS, and ZnO-ZnS NR array photo-electrodes under (a) dark and (b) visible light illumination conditions recorded over the frequency range from 2 Hz to 100 kHz.



**Fig. 12.** Trapping experiment of active species during the photocatalytic reaction with 75 min Xe lamp irradiation.
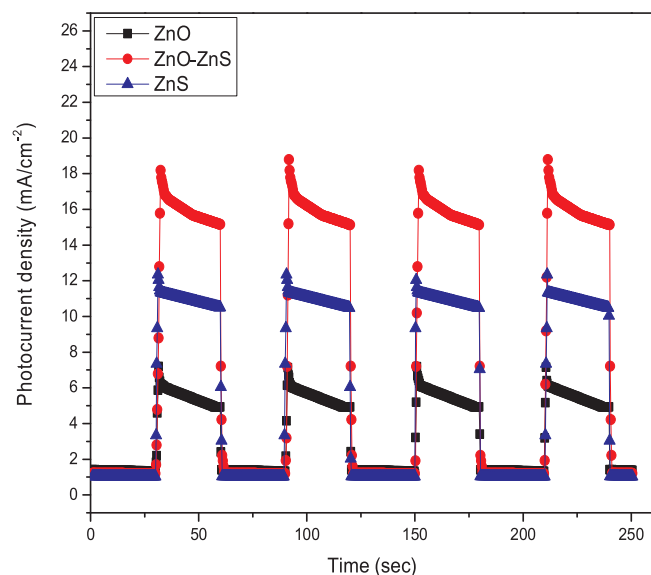


**Fig. 11.** Amperometric J–t curves of the pristine ZnO, ZnS and ZnO-ZnS core shell NR array photo-electrodes measured at 2 V vs. Ag/AgCl under visible light on-off cycles.

The above results indicate that the sulfidation process has a great effect on the relative intensity and position of typical PL properties of ZnO nanocrystals. Therefore, the PL properties of ZnO nanocrystals could be tuned by this approach. Survey-scanned XPS spectrum of the hierarchical NR samples, and the Zn 2p, S 2p, and O 1 s binding energies of the photocatalyst were investigated by X-ray photoelectron spectroscopy (XPS) to investigate the surface composition and chemical states of the ZnO NRs and ZnO-ZnS (8 h) NR core shell NRs, as shown in Fig. 8. The Fig. 8a shows the survey spectrum of the shell wall controlled ZnO-ZnS core shell NR arrays. Fig. 8b shows the XPS O 1 s state of the shell wall controlled ZnO-ZnS core-shell NR arrays. The presence of lattice oxygen located at 530.2 eV indicate the formation of Zn-O. Additional peaks located at 531.4 eV and 532.3 eV can be assigned to the oxygen vacancies and chemisorbed oxygen of surface hydroxyl groups respectively. In comparison with pure ZnO nanorods, a suppression of the lattice oxygen peak at 530.1 eV is observed after the growth of ZnS shell layer. XPS spectrum of S 2p and Zn 2p peaks of shell wall controlled ZnO-ZnS core-shell nanorods are plotted in Fig. 8c, d respectively. The peak at 160.8 eV is assigned to S 2p (Fig. 8c), indicating that the shell layer consists of ZnS. Deconvolution of these chemical species was performed using a Gaussian function to fit S $2p^{3/2}$ and S $2p^{1/2}$ peaks for sulfide and thiolate. The Fig. 8d reveals the Zn $2p^{5/2}$ and Zn $2p^{3/2}$ peaks are observed at 1021.7 and 1044.8 eV, respectively, which are similar to the reported ZnO nanostructures. The XPS analysis reveals the composition and chemical states of ZnO-ZnS core-shell nanorods.

### 3.3. Photocatalytic properties

Figs. 9 and S5 displays the photodegradation efficiency of as-prepared ZnO NRs and different shell wall thickness grown ZnO-ZnS coreshell NRs against MB under UV, simulated visible source and natural sunlight irradiation. On irradiating the ZnO based nanostructures under visible irradiation, they exhibited MB decomposition levels of 64.4%, 96.3%, 98.7%, 98.3%, 98.21%, 93.9% and 87.4% for ZnO NRs, ZnO-ZnS NRs (4 h), ZnO-ZnS NRs (8 h), ZnO-ZnS NRs (12 h), ZnO-ZnS NRs (16 h), and ZnO-ZnS NRs (20 h) core-shell morphologies respectively in 135 min. Similar trend on catalytic efficiency with the different shell wall thickness were obtained under UV and natural sunlight irradiation. Table. 1 records the photoresponsive properties of shell wall controlled ZnO-ZnS based core-shell NR arrays. As compared to the bare ZnO NR array, 8 h sulfidated ZnO-ZnS based core shell NR arrays show higher visible catalytic activity. It also shows that the photocatalytic activity of the hybrid nanostructures first tends to increase and then decreases with the increase in thickness of ZnS shell layer. ZnO-ZnS core-shell

observed for ZnO-ZnS structure could be the superposition of two individual emissions from the core-shell structure. Along with the green emission (from ZnO), additional peak in the orange region (620 nm) could be associated with ZnS layer. In contrast, the PL spectrum of ZnS (20 h sulfidated ZnO) nanorods exhibit only a broad weak peak centered at about 512 nm, similar to the reported PL characteristics of other ZnS nanostructures. [39] From the above observation, we can conclude that the intensity of visible emission was obviously enhanced after a thin layer of ZnS was coated on ZnO nanorods. Therefore, these ZnO-ZnS core-shell nanorods are more applicable for the fabrication of visible photocatalytic systems.

As we know, the green emissions originate from oxygen interstitials and vacancies. During the process of the formation of ZnO-ZnS coreshell structures, the hydrolysis of TAA can produce $H_2S$ and sulphur atom can replace and squeeze out the oxygen interstitials and vacancies from the surface of ZnO nanocrystals. As a result, the concentration of oxygen interstitials reduces greatly and the green emission is weakened.
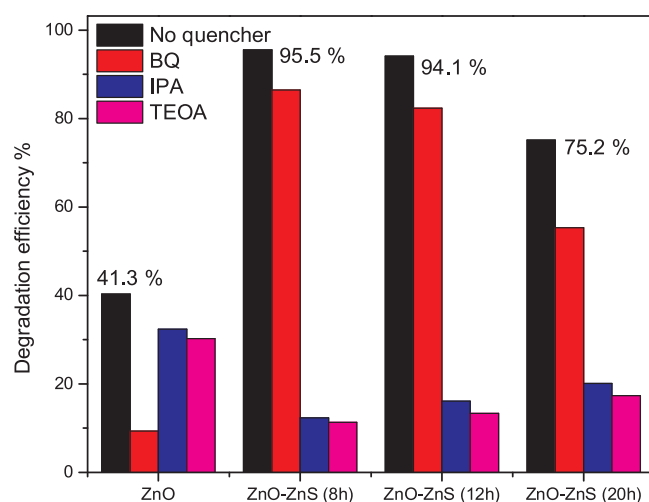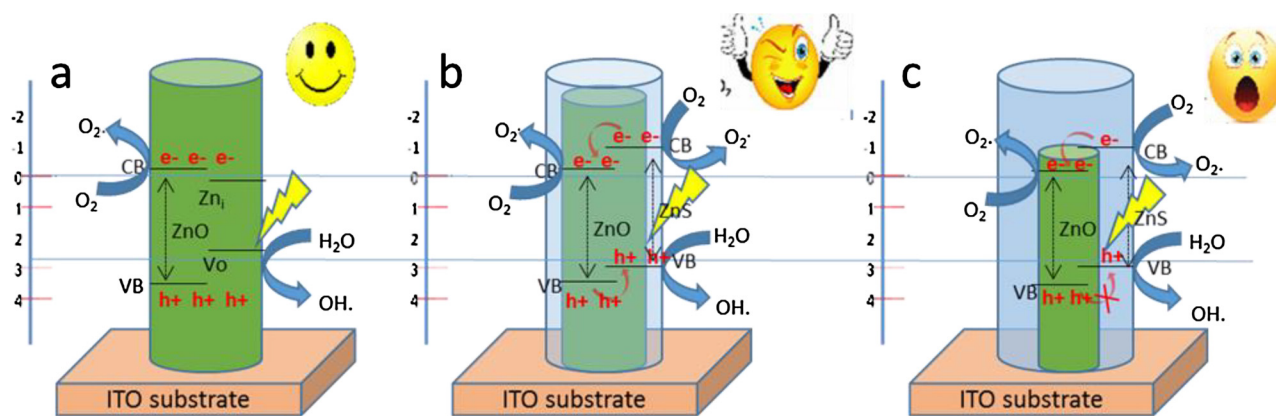
**Fig. 13.** Schematic representation of the photocatalytic mechanism on shell wall varied ZnO-ZnS heterostructured photocatalysts.

arrays having the shell wall thickness of ∼ 20 nm synthesized in 8 h of sulfidation shows the maximum photocatalytic efficiency, indicating that shell wall thickness is critical for enhancing the catalytic performance. Fig. 9 b shows the kinetics plot of shell wall controlled ZnO-ZnS core shell NR arrays for MB photodegradation. Upon varying the ZnS wall thickness, the plot of $ln(C/C_0)$ against the irradiation time (t) is nearly a straight line, in which the slope of the fitting line is equal to the value of rate constant. The corresponding kinetic constants with different shell wall controlled NR arrays are shown in Fig. 9c. In visible irradiation, the highest apparent rate constant under our experimental conditions is determined to be $0.04187 \, min^{-1}$ for 8 h sulfidated ZnO-ZnS core shell NR arrays having 20 nm of shell wall thickness, which is about 6 times, 3 times and 21 times higher than that of pure ZnO NR arrays $(0.00704 \, min^{-1})$, ZnS (20 h sulfidated) NR arrays $(0.01542 \, min^{-1})$ and ZnO buffer layer $(0.00197 \, min^{-1})$, respectively, revealing the superior visible photocatalytic activity for core-shell hierarchical NR arrays. Catalytic efficiency over the RhB dye (15 ppm) was of similar trend as the shell wall controlled ZnO-ZnS core shell NR arrays.

### 3.4. Photo responsive properties

Electrochemical impedance spectroscopy (EIS) was employed to investigate the charge-carrier migration and effective charge separation on the catalytic surface under photo-responsive behavior. The photoelectrochemical properties were investigated over the pristine ZnO, 8 h sulfidated ZnO-ZnS (which has the superior catalytic behavior), and 20 h sulfidated ZnO-ZnS (which shows the exhibition of ZnS NR) core shell NR arrays. Here, EIS has been performed to study the photogenerated charge separation processes and the electrical conductivity of pristine ZnO NRs, 8 h, and 20 h sulfidated ZnO-ZnS core-shell NRs under dark and visible light illumination conditions, as shown in Fig. 10. The equivalent series resistance (ESR) provided by the intercept on the real axis in the high frequency range, which arises the inherent resistances of the photoactive material used as the photo-electrode, bulk resistance of electrolyte, and the contact resistance at the interface between the electrolyte and the photoelectrode. Under the photo illumination, the magnitudes of the ESR obtained for ZnO-ZnS core-shell NRs have higher electrical conductivity than the pristine ZnO NR arrays. The electron transfer resistance at the surface of the electrodes can be represented from the radius of the arc in the high frequency region of the EIS spectrum which resulting from the diffusion of electrons [40,41]. The arcs of EIS Nyquist plots for the ZnO NRs and ZnS modified ZnO core-shell NRs clearly indicate that charge transfer occurs in the photo-electrodes. From the EIS plot in Fig. 10, it is clearly evident that the arc radii of the ZnO-ZnS core-shell NRs are higher than those of the pristine ZnO NRs under dark conditions. It evidences that by modifying the ZnS as a shell over ZnO NR arrays, slightly restricts

electron transport through the NRs. But as a function of light irradiation, the arc radius of the EIS spectra of the ZnO-ZnS core-shell NRs is nearly equal to the ZnO NRs under visible light illumination, which suggests that the ZnS nano-shell leads to a more effective charge separation and a faster interfacial charge transfer, providing an ideal pathway for electron transport to the current collector (ITO) [42,43]. The EIS studies reveal that on introduction of the thin ZnS nano-shell to the ZnO NRs core significantly improves the photogenerated charge separation under visible light illumination and helps in the faster electron transport through the NRs photoanode.

The current density versus potential (J−V) curves of the ZnO, 8 h and 20 h of sulfidated ZnO-ZnS core shell NR photoelectrode arrays was recorded in the dark and under visible light illumination (l > 400 nm) at room temperature. The J−V curve of the pure ZnO NR arrays shows low current density of $1.18 \, mA \, cm^{-2}$ at a potential of 1 V. It also clears that the photoresponse of the pure ZnO NRs photoanode is very weak, and the current density increases only by 1.3 fold (from 1.03 to $1.42 \, mA \, cm^{-2}$ at a potential of 1 V vs. Ag/AgCl) when the photo-electrode is illuminated by visible light. The 8 h sulfidated ZnO-ZnS core-shell NRs show a dark current density of $1.36 \, mA \, cm^{-2}$ at a potential of 1 V vs. Ag/ AgCl. Upon visible light illumination, the current density increases significantly to $2.846 \, mA \, cm^{-2}$ at a potential of 1 V vs. Ag/ AgCl. This shows a 1.3 fold increase in the current density of NRs over the measurement performed under the dark condition, indicating the enhanced photoelectrochemical performance of the ZnO-ZnS core-shell NRs over the pristine ZnO NRs. Fig. 11 shows the amperometric J–t curves of the pristine ZnO, ZnO-ZnS (8 h sulfidated) and ZnS (20 h sulfidated) NR arrays photoanodes recorded at a potential of 2 V vs. Ag/ AgCl with the illumination 'on' and 'off'. It evidences that the response in current density during the 'on' and 'off' of the photo illumination in ZnO-ZnS core-shell NRs is very prominant, unlike the photo switching response of ZnO NR arrays which is very slow between the two states. From Fig. 11, it was found that ZnO-ZnS core-shell NR arrays have noticeable improvement in visible light response over the pristine ZnO NR arrays. On increasing the shell wall thickness, the 20 h sulfidated ZnO NR arrays shows decreased photo response when compared with the 8 h sulfidated ZnO-ZnS core-shell NR arrays. The admirable photoresponse of the NR arrays electrodes to the on-off cycling admit that the effective charge transport between the ZnO-ZnS core-shell takes place rapidly. It pointout that the thin ZnS shell and the ZnO-ZnS interface significantly enhance the visible light absorption efficiency and the efficient charge separation at the interface, which results together with superior photoelectrochemical properties. The small values of built-in voltage between $Vbi_{(ZnO)}$ and $Vbi_{(ZnS)}$ suggest that the relative injection of electrons and holes at the heterointerface are almost nearly same. The contact between ITO substrate and ZnO is ohmic by nature, as the work function of ITO (4.5 eV) is less than that of the ZnO. Therefore, when the systematically constructed heterostructural arrays

were subjected to a positive bias, the electrons of the CB of the ZnS can easily enter into the CB of the ZnO, and finally the electrons get collected by the current collector [ITO substrate]. Here the solution grown 1D vertically aligned ZnO NRs are gifted with a large surface area, and therefore the core-shell structure also offers a large interface between the ZnO core and the ZnS shell. The surface contains a lot of surface states due to incomplete covalent bonds and other effects other than bloch-state bands. These surface states act as donors and lie in the bulk band gap of ZnO and ZnS. Number of interface states were raised by the larger interface [44] near the conduction band edge in the semiconductor band gap, resulting from the interfacial stress due to lattice mismatch at the heterojunction. It create the good possibility for pinning of fermi level near the conduction band edge. These surface and interface states coupled with other defect states make these NRs sensible to visible light (as also evidenced from the UV–vis absorption spectra), even though the heterostructures are constituents of wide band gap semiconductors.

The sharper visible photo-switching response of the ZnO-ZnS NRs photoelectrode is also observed, as the photogenerated excitons in the system rapidly decompose into their constituent particles at the NRs interface resulting in the fast injection of electrons into the CB of ZnO because of the interfacial band alignment, and thus the heterojunction can reduce the recombination of photoinduced electron–hole pairs and consequently increase the photocurrent response of the NRs. But the higher shell wall grown ZnO-ZnS (20 h) core shell NR arrays resulted in decreased photocurrent response. In this study, the increased photoresponse reveals that the photoinduced electrons and holes can be separated effectively and as well as the recombination of the electron-hole pairs is hindered. The current increased rapidly under light irradiation and recovers quickly when the light is turned off, thus the reversible and stable photocurrent response of the photocatalysts is observed. These photocurrent results are consistent with the photocatalytic activity results. The photocurrent decreased with further increase of shell wall thickness after 8 h of sulfidation. These photocurrent response trends were consistent with the observed photocatalytic activity results of ZnO-ZnS nanorods based photocatalysts. The enhanced photoresponse indicated effective separation of photogenerated electrons and holes.

### 3.5. Proposed photocatalytic mechanism

The significant photo responsivity over the shell wall tunable hybrid composite catalysts motivates us to further study the photocatalytic reaction mechanism of the degradation process. Fig. 12 displays the trapping experiment of active species during the photocatalytic reaction of pristine and 8 h and 20 h sulfidated ZnO-ZnS core-shell NR arrays under visible irradiation. Generally, photo induced holes ($h^+$), hydroxyl radicals ($°OH$) and superoxide radicals ($°O_2$) are known to be the main reactive species involved in the photodegradation reaction. [30,31] In our radical trapping experiments, 1 mmol $L^{-1}$ of isopropanol (IPA), 1,4-benzoquinone (BQ) and triethanolamine (TEOA) were added into MB solution and used as a hydroxyl radical, superoxide radical and hole scavengers during the catalytic process in order to understand the mechanism behind their catalytic property (Fig. 12). For pristine ZnO NR arrays, the photocatalytic degradation activities for MB decrease remarkably by the adding of BQ. However, when IPA and TEOA are added, the activity is also declined, but not as significant as that with BQ added. These results suggest that, production of superoxide radicals are the major responsible ROS in the ZnO during the catalytic activity. For 8 h, 12 h and 20 h sulfidated ZnO-ZnS core shell NR arrays, this trend gets reversed and addition of the IPA and TEOA majorly influence the catalytic behavior which reveals the photo generated holes and the hydroxyl radicals are the more active species in the ZnO-ZnS based core shell system. However, when BQ was added, there is no significant decrease in catalytic activity in the core shell system. In addition ZnO-ZnS system (8 h, 12 h and 20 h sulfidated ZnO NR arrays) exhibit similar

ratio on the production of superoxide and hydroxyl radicals, but the production rate of ROS was higher in the lower shell wall grown ZnO-ZnS (8 h) core shell NR array catalyst which improvised its catalytic behavior.

Based on above experimental results, a possible mechanism has been proposed for the enhanced visible-light activity of ZnO-ZnS hierarchical core-shell catalysts and a schematic diagram is illustrated in Fig. 13. As the ZnO and ZnS are the wide band gap semiconductors both in the pure form can't be excited by visible light and produce photoinduced electrons and holes. But the recent theoretical and experimental results predict that, band energies were reduced at the ZnO-ZnS core-shell interface as low as 2.07 eV [45] which is influenced by the interfacial lattice strain that occur along the interface of type II ZnO-ZnS heterostructure. [46] The thickness of the shell wall pronounces the effective separation of charge carriers which determine the catalytic efficiency. In ZnO-ZnS core-shell arrays, both the bottom of the conduction band (CB) and the top of the valence band (VB) of ZnS (-0.96 eV and 2.84 eV vs. NHE, pH = 7) are more negative than that of ZnO core (-0.32 eV and 2.98 eV vs. NHE, pH = 7). Thus the photogenerated electrons could transfer easily from ZnS into the CB of ZnO, while the holes could migrate from ZnO into the VB of ZnS via the interface of the heterojunction. It's well known that the electron affinities ($E_a$) of ZnO and ZnS are 4.5 and 3.9 eV, respectively [47]. Therefore, an upward band offset of 0.6 eV between conduction bands of ZnO and ZnS exists in the energy band diagram of the ZnO-ZnS NRs (Fig. 13b). It offer the redistribution of charge carrier on each side of the heterojunction (as shown in Fig. 13) which significantly hinders the recombination process of electron-hole pairs and improves the efficiency of interfacial charge separation.

We believe that the spatial separation of the carriers reduces the recombination probability of the photogenerated electron and hole pairs. But the shell wall layer in the form of nano grained assembly may have lot of trap states which initiate the carrier recombination. As observed from the results from the trapping experiments, photo generated holes and the °OH are the major active components in the core shell system for the photocatalytic degradation. Visible absorption behavior in the ZnO-ZnS core shell will be attained at the core shell interface. As the hole mobility in the ZnS (5 cm$^2$/Vs) is very low as compared with its electron mobility (180 cm$^2$/Vs), on increasing the shell wall thickness, photo generated holes travel longer distance which initiates the carrier recombination process. Optimum thin shell layer (~ 20 nm) 8 h sulfidated ZnO-ZnS NR arrays show higher photocatalytic activity which reveals that the photo responsivity of the ZnO-ZnS core-shell NR arrays are represented by its shell wall thickness. Thin shell layers ZnO-ZnS (8 h) NR arrays effectively produces and separated the charge carriers than the 12 h, 16 h and 20 h sulfidated ZnO-ZnS NR arrays which improvised its catalytic behaviour. In 4 hours sulfidation, very thin layer heterojunction interface and poor barrier potentials reveals the slower photocatalytic efficiency than the 8 h sulfidated ZnO-ZnS NR arrays. Further, the constructed core-shell system were assembled by nanograins with polycrystalline nature. Thus the holes has to cross over several grain boundaries to reach the surface. Several grain boundaries at the shell layer could trap more number of photo generated holes by the recombination process which would delay the catalytic activity. Fig. S6 shows the catalytic degradation performances of recycled photocatalysts during five repeated tests. During the five repeated degradation cycles, limited activity loss was observed for ZnO-ZnS nanorods based photocatalyst. The degradation efficiency rate for the fifth test was 92.6% of the first test with the stable strucral and morphological finish (Fig. S7). These ZnO-ZnS core–shell nanorods based photocatalysts exhibited high visible photocatalytic activity and good stability.

### 4. Conclusion

Formation of shell wall controlled ZnO-ZnS core-shell nanorod

arrays on ITO substrates favors the absorption of light and the separation of photogenerated electron-hole pairs, and contact between the reactant solution and the photocatalysts, leading to efficient photocatalytic activity. The thickness of the ZnS shell have great influence on the photocatalytic performance of the ZnO-ZnS core-shell nanorods based immobilized hierarchical photocatalyst. The maximum degradation rate of ZnO-ZnS nanorod array based hierarchical photocatalyst reached 0.0205, 0.0419 and 0.0225 min$^{-1}$ under UV, Visible and natural solar light irradiation. The amount of degradation efficiency for the fifth test is 92.6% of the first test. The optimized ZnO-ZnS core-shell NR arrays having the shell wall thickness of 20 nm exhibited high photocatalytic activity and good stability in dye degradation.

## Acknowledgement

## Appendix A. Supplementary data

Supplementary material related to this article can be found, in the online version, at doi:https://doi.org/10.1016/j.apcatb.2018.03.099.

## References

[1] K.J. Choi, H.W. Jang, One-Dimensional oxide nanostructures as gas-sensing materials: review and issues, Sensors 10 (2010) 4083–4099.
[2] Y. Liu, X. Dong, P. Chen, Biological and chemical sensors based on graphene materials, Chem. Soc. Rev. 41 (2012) 2283–2307.
[3] H. Sun, J. Deng, L. Qiu, X. Fang, H. Peng, Recent progress in solar cells based on one-dimensional nanomaterials, Energy Environ. Sci. 8 (2015) 1139–1159.
[4] L. Sang, M. Liao, M. Sumiya, A comprehensive review of semiconductor ultraviolet photodetectors: from thin film to one-dimensional nanostructures, Sensors. 13 (2013) 10482–10518.
[5] Y.Q. Zheng, J.Y. Wang, J. Pei, One-dimensional (1D) micro/nanostructures of organic semiconductors for field-effect transistors, Sci. China Chem. 58 (2015) 937–946.
[6] F. Léonard, A.A. Talin, Electrical contacts to one- and two-dimensional nanomaterials, Nat. Nanotechnol. 6 (2011) 773–783.
[7] V.J. Babu, S. Vempati, T. Uyar, S. Ramakrishna, Review of one-dimensional and two-dimensional nanostructured materials for hydrogen generation, Phys. Chem. Chem. Phys. 17 (2015) 2960–2986.
[8] F.X. Xiao, J. Miao, H.B. Tao, S.F. Hung, H.Y. Wang, One-Dimensional hybrid nanostructures for heterogeneous PhotocatalysFis and photoelectrocatalysis, Small 11 (2015) 2115–2131.
[9] J.H. Pan, H. Dou, Z. Xiong, C. Xu, J. Ma, X.S. Zhao, Porous photocatalysts for advanced water purifications, J. Mater. Chem. 20 (2010) 4512–4528.
[10] M.M. Montero, A.N. Filippin, Z. Saghi, F.J. Aparicio, A. Barranco, J.P. Espinos, F. Frutos, A.R.G. Elipe, A. Borras, Vertically aligned hybrid Core/Shell semiconductor nanowires for photonics applications, Adv. Funct. Mater. 23 (2013) 5981–5989.
[11] S. Dong, J. Feng, M. Fan, Y. Pi, L. Hu, X. Han, M. Liu, J. Sun, J. Sun, Recent developments in heterogeneous photocatalytic water treatment using visible light responsive photocatalysts: a review, RSC Adv. 5 (2015) 14610–14630.
[12] X. Chen, S. Shen, L. Guo, S.S. Mao, Semiconductor-based photocatalytic hydrogen generation, Chem. Rev. 110 (2010) 6503–6570.
[13] S. Girish Kumar, K.S.R. Koteswara Rao, Zinc oxide based photocatalysis: tailoring surface-bulk structure and related interfacial charge carrier dynamics for better environmental applications, RSC Adv. 5 (2015) 3306–3351.
[14] K.M. Lee, C.W. Lai, K.S. Ngai, J.C. Juan, Recent developments of zinc oxide based photocatalyst in water treatment technology: a review, Water Res. 88 (2016) 428–448.
[15] S. Sarkar, D. Basak, Self-Powered highly enhanced dual wavelength ZnO@CdS core–shell nanorod arrays photodetector: an intelligent pair, ACS Appl. Mater. Interfaces 7 (2015) 16322–16329.
[16] M.E. Fragala, I. Cacciotti, Y. Aleeva, R. Lo Nigro, c A. Bianco, G. Malandrino, C. Spinella, G. Pezzottid, G. Gusmano, Core–shell Zn-doped TiO2–ZnO nanofibers fabricated via a combination of electrospinning and metal–organic chemical vapour deposition, Cryst. Eng. Comm. 12 (2010) 3858–3865.
[17] L. Shi, Y. Xu, S. Hark, Y. Liu, S. Wang, L.M. Peng, K. Wong, Q. Li, Optical and electrical performance of SnO2capped ZnO nanowire arrays, Nano Lett. 7 (2007) 3559–3563.
[18] C.M. Lung, W.C. Wang, C.H. Chen, L.Y. Chen, M.J. Chen, ZnO/Al2O3core/shell nanorods array as excellent anti-reflection layers on silicon solar cells, Mater. Chem. Phys. 180 (2016) 195–202.
[19] X. Chen, Z. Bai, X. Yan, H. Yuan, G. Zhang, P. Lin, Z. Zhang, Y. Liu, Y. Zhang, Design of efficient dye-sensitized solar cells with patterned ZnO-ZnS core-shell nanowire array photoanodes, Nanoscale 6 (2014) 4691–4697.
[20] S. Yang, L. Wang, Y. Wang, L. Li, T. Wang, Z. Jiang, Identification and characteristics of ZnO/MgO core–shell nanowires, AIP Adv. 5 (2015) 037122.
[21] X. Mo, G. Fang, H. Long, S. Li, H. Wang, Z. Chen, H. Huang, Y. Zeng, Y. Zhang, C. Pan, Unusual electroluminescence from n-ZnO@i-MgO core–shell nanowire color-tunable light-emitting diode at reverse bias, Phys. Chem. Chem. Phys. 16 (2014) 9302–9308.
[22] F. Mirnajafizadeh, F. Wang, P. Reece, J.A. Stride, Synthesis of type-II CdSe(S)/Fe2O3core/shell quantum dots: the effect of shell on the properties of core/shell quantum dots, J. Mater. Sci. 51 (2016) 5252–5258.
[23] J. Lahiri, M. Batzill, Surface functionalization of ZnO photocatalysts with monolayer ZnS, J. Phys. Chem. C. 112 (2008) 4304–4307.
[24] J. Schrier, D.O. Demchenko, L.W. Wang, Optical properties of ZnO/ZnS and ZnO/ZnTe heterostructures for photovoltaic applications, Nano Lett. 7 (2007) 2377–2382.
[25] Sunghoon Park, Soohyun Kim, Hyunsung Ko, Chongmu Lee, Light-enhanced gas sensing of ZnS-core/ZnO-shell nanowires at room temperature, J. Electroceram. 33 (1) (October 2014) 75–81.
[26] M.H. Hsu, C.J. Chang, H.T. Weng, Efficient H2production using Ag2s-coupled ZnO@ZnS core–shell nanorods decorated metal wire mesh as an immobilized hierarchical photocatalyst, ACS Sustain. Chem. Eng. 4 (2016) 1381–1391.
[27] J. Rouhi, M.H. Mamat, C.H. Raymond Ooi, S. Mahmud, M.R. Mahmood, High-Performance dye-sensitized solar cells based on morphology-controllable synthesis of ZnO–ZnS heterostructure nanocone photoanodes, PLoS One 10 (2015) e0123433.
[28] K.S. Ranjith, P. Saravanan, V.T.P. Vinod, J. Filip, M. Cerník, R.T. Rajendra Kumar, Ce2S3decorated ZnO-ZnS core-shell nanorod arrays: efficient solar-driven photocatalytic properties, Catal. Today 278 (2016) 271–279.
[29] K.S. Ranjith, R. Pandian, E. McGlynn, R.T. Rajendra Kumar, Alignment, morphology and defect control of vertically aligned ZnO nanorod array: competition between "Surfactant" and "Stabilizer" roles of the amine species and its photocatalytic properties, Cryst. Growth Des. 14 (2014) 2873–2879.
[30] L. Ye, K. Deng, F. Xu, L. Tian, T. Peng, L. Zan, Increasing visible-light absorption for photocatalysis with black BiOCl, Phys. Chem. Chem. Phys. 14 (2012) 82–85.
[31] Y. Bai, P.Q. Wang, J.Y. Lin, X.J. Lin, Enhanced photocatalytic performance of direct z-scheme BiOCl-g-C3N4 photocatalysts, RSC Adv. 4 (2014) 19456–19461.
[32] Y. Hu, H. Qian, Y. Liu, G. Du, F. Zhang, L. Wang, X. Hu, A microwave-assisted rapid route to synthesize ZnO/ZnS core–shell nanostructures via controllable surface sulfidation of ZnO nanorods, Cryst. Eng. Comm. 13 (2011) 3438–3443.
[33] H.Q. Wu, Q.Y. Wang, Y.Z. Yao, C. Qian, X.J. Zhang, X.W. Wei, Microwave-Assisted synthesis and photocatalytic properties of carbon nanotube/Zinc sulfide heterostructures, J. Phys. Chem. C. 112 (2008) 16779–16783.
[34] X.M. Shuai, W.Z. Shen, A facile chemical conversion synthesis of ZnO/ZnS Core/Shell nanorods and diverse metal sulfide nanotubes, J. Phys. Chem. C. 115 (2011) 6415–6422.
[35] S.K. Panda, A. Dev, S. Chaudhuri, Fabrication and luminescent properties of c-Axis oriented ZnO-ZnS core-shell and ZnS nanorod arrays by sulfidation of aligned ZnO nanorod arrays, J. Phys. Chem. C. 111 (2007) 5039–5043.
[36] J. Yan, X. Fang, L. Zhang, Y. Bando, U.K. Gautam, B. Dierre, T. Sekiguchi, D. Golberg, Structure and cathodoluminescence of individual ZnS/ZnO biaxial nanobelt heterostructures, Nano Lett. 8 (2008) 2794–2799.
[37] D. Liu, Y. Lv, M. Zhang, Y. Liu, Y. Zhu, R. Zong, Y. Zhu, Defect-related photoluminescence and photocatalytic properties of porous ZnO nanosheets, J. Mater. Chem. A. 2 (2014) 15377–15388.
[38] Y.F. Zhu, D.H. Fan, W.Z. Shen, A General chemical conversion route to synthesize various ZnO-Based Core/Shell structures, J. Phys. Chem. C. 112 (2008) 10402–10406.
[39] G.J. Lee, S. Anandan, S.J. Masten, J.J. Wu, Sonochemical synthesis of hollow copper doped zinc sulfide nanostructures: optical and catalytic properties for visible light assisted photosplitting of Water, Ind. Eng. Chem. Res. 53 (2014) 8766–8772.
[40] Z. Wang, X. Zhan, Y. Wang, M. Safdar, M. Niu, J. Zhang, Y. Huang, J. He, ZnO/ZnSxSe1-x core/shell nanowire arrays as photoelectrodes with efficient visible light absorption, Appl. Phys. Lett. 101 (2012) 073105.
[41] X. Xia, J. Tu, Y. Zhang, X. Wang, C. Gu, X.-B. Zhao, H.J. Fan, High-quality metal oxide core/shell nanowire arrays on conductive substrates for electrochemical energy storage, ACS Nano 6 (2012) 5531–5538.
[42] X. Pan, C.H. Chen, K. Zhu, Z.Y. Fan, TiO2 nanotubes infiltrated with nanoparticles for dye sensitized solar cells, Nanotechnology 22 (2011) 235402..
[43] A. Sarkar, A.K. Singh, G.G. Khan, D. Sarkar, K. Mandal, TiO2/ZnO core/shell nanoheterostructure arrays as photo-electrodes with enhanced visible light photoelectrochemical performance, RSC Adv. 4 (2014) 55629–55634.
[44] B. Cheng, G. Wu, Z. Ouyang, X. Su, Y. Xiao, S. Lei, Effects of interface States on photoexcited carriers in ZnO/Zn2SnO4 type-ii radial heterostructure nanowires, ACS Appl. Mater. Interfaces 6 (2014) 4057–4062.
[45] Z. Wang, S.W. Cao, S.C.J. Loo, C. Xue, Nanoparticle heterojunctions in ZnS-ZnO hybrid nanowires for visible-light-driven photocatalytic hydrogen generation, Cryst. Eng. Comm. 15 (2013) 5688–5693.
[46] S.C. Rai, K. Wang, Y. Ding, J.K. Marmon, M. Bhatt, Y. Zhang, W. Zhou, Z.L. Wang, Piezo-phototronic effect enhanced UV/Visible photodetector based on fully Wide band gap type-ii ZnO/ZnS Core/Shell nanowire array, ACS Nano 9 (2015) 6419–6427.
[47] M.Y. Lu, J. Song, M.P. Lu, C.Y. Lee, L.J. Chen, Z.L. Wang, ZnO-ZnS heterojunction and ZnS nanowire arrays for electricity generation, ACS Nano 3 (2009) 357–362.